

Intelligent Omni-Surfaces: Reflection-Refraction Circuit Model, Full-Dimensional Beamforming, and System Implementation

Shuhao Zeng, *Student Member, IEEE*, Hongliang Zhang, *Member, IEEE*,

Boya Di, *Member, IEEE*, Yuanwei Liu, *Senior Member, IEEE*,

Marco Di Renzo, *Fellow, IEEE*, Zhu Han, *Fellow, IEEE*,

H. Vincent Poor, *Life Fellow, IEEE*, and Lingyang Song, *Fellow, IEEE*

Abstract

The intelligent omni-surface (IOS) is a dynamic metasurface that has recently been proposed to achieve full-dimensional communications by realizing the dual function of anomalous reflection and anomalous refraction. Existing research works provide only simplified models for the reflection and refraction responses of the IOS, which do not explicitly depend on the physical structure of the IOS and the angle of incidence of the electromagnetic (EM) wave. Therefore, the available reflection-refraction models are insufficient to characterize the performance of full-dimensional communications. In this paper, we propose a complete and detailed circuit-based reflection-refraction model for the IOS, which is formulated in terms of the physical structure and equivalent circuits of the IOS elements, as well as we validate it against full-wave EM simulations. Based on the proposed circuit-based model for the IOS, we analyze the asymmetry between the reflection and transmission coefficients. Moreover, the proposed circuit-based model is utilized for optimizing the hybrid beamforming of IOS-assisted networks and hence improving the system performance. To verify the circuit-based model, the theoretical findings, and to evaluate the performance of full-dimensional beamforming, we implement a prototype of IOS and deploy an IOS-assisted wireless communication testbed to experimentally measure the beam patterns and to quantify the achievable rate. The obtained experimental results validate the theoretical findings and the accuracy of the proposed circuit-based reflection-refraction model for IOSs.

Index Terms

S. Zeng, B. Di, and L. Song are with School of Electronics, Peking University, Beijing 100871, China (email: shuhao.zeng@pku.edu.cn; boya.di@pku.edu.cn; lingyang.song@pku.edu.cn).

H. Zhang and H. V. Poor are with Department of Electrical and Computer Engineering, Princeton University, Princeton, NJ 08544, USA (email: hz16@princeton.edu, poor@princeton.edu).

Y. Liu is with the School of Electronic Engineering and Computer Science, Queen Mary University of London, London E1 4NS, U.K. (e-mail: yuanwei.liu@qmul.ac.uk).

M. Di Renzo is with Université Paris-Saclay, CNRS, CentraleSupélec, Laboratoire des Signaux et Systèmes, 3 Rue Joliot-Curie, 91192 Gif-sur-Yvette, France. (marco.di-renzo@universite-paris-saclay.fr)

Z. Han is with Electrical and Computer Engineering Department, University of Houston, Houston, TX, USA, and also with the Department of Computer Science and Engineering, Kyung Hee University, Seoul, South Korea (email: zhan2@uh.edu).

Intelligent omni-surface, circuit-based reflection-refraction model, full-dimensional beamforming, prototype.

I. INTRODUCTION

The enormous increase of mobile devices and applications in the past decade has triggered the needs for new communication paradigms and technologies [1]. Notably, to support high-speed and seamless data services in future wireless systems, a variety of transmission techniques that exploit the implicit randomness of the wireless environment have received increasing attention, such as spatial modulation [2] and massive multiple input and multiple output (MIMO) systems [3]. However, multiple-antenna technologies usually require a high hardware cost and power consumption, and need complex signal processing algorithms [4]–[6]. Existing techniques, in addition, only adapt themselves to the wireless propagation environment. Therefore, the quality of service cannot always be guaranteed in harsh propagation environments, e.g., when the line-of-sight links are blocked at high frequency bands [7], [8].

Thanks to the recent developments and research advances in the field of metasurfaces, a new wireless technology named *reconfigurable intelligent surface* (RIS) is being developed, which is intended to turn the wireless propagation environment into a programmable entity for further improving the performance of state-of-the-art technologies in challenging propagation environments [9], [10]. Specifically, an RIS is an ultra-thin surface consisting of multiple subwavelength scattering elements [11], which can apply an adjustable amplitude and phase shift to the incident electromagnetic (EM) waves [12], [13]. A typical implementation of an RIS comprises several scattering elements with integrated electronic circuits, such as positive-intrinsic-negative (PIN) diodes or varactors [14], [15]. By controlling the ON/OFF status of the PIN diodes or the biasing voltages of the varactors, the amplitude and the phase of the incident EM waves can be adjusted [16], [17]. Benefiting from this programmable feature, an RIS can shape the propagation environment into a desirable form, and can hence improve the link quality and the coverage even in harsh and challenging propagation environments [8], [10]. In addition, an RIS has the appealing attribute of shaping the wireless environments without requiring power amplifiers, digital processing units for signal regeneration, and multiple radio frequency chains. Even though some power is still needed to make the surface reconfigurable [18], these characteristics may reduce the total power consumption and the hardware cost as compared with other technologies. Some examples are available in [19]–[21]. These features collaboratively make an RIS a promising technology for future wireless networks, but they result in some design

and deployment challenges, which include how to efficiently estimate the channel and how to optimize the RISs in a scalable manner, see, e.g., [5], [9].

The vast majority of research works conducted in the field of RIS-aided communications have considered RISs that operate in reflection mode. In other words, the RIS is designed to reflect the signals that impinge on one side of the surface towards user equipments (UEs) that are located on the same side, while the transmitted signal is minimized [12]. This implementation is also referred to as intelligent reflecting surface (IRS). Because of the reflection characteristics of the IRS, however, the UEs located on the opposite side of the surface are out of coverage. Use cases where UEs located on the side of the surface that is not illuminated by the transmitter may benefit from the deployment of an RIS have recently been reported in [20]. Motivated by these considerations, an RIS design that is referred to as intelligent omni-surface (IOS) has recently been introduced [22]. In the literature, this design of RIS is also referred to as simultaneously transmitting and reflecting RIS (STAR-RIS) [24]. In contrast to an IRS, an IOS has the dual functionality of reflection and refraction, which makes it capable of providing ubiquitous coverage to the UEs located on both sides of the surface, so as to achieve full-dimensional wireless communications.

The existing works on IOSs are limited in number and are focused on physical and channel modeling [23], [24], beamforming design [22], [25]–[27], and performance analysis [28], [29]. Specifically, several IOS hardware and channel models as well as the available hardware implementations are overviewed in [23], which serve as a physics-compliant pipeline for further investigations. In [24], signal models and operation protocols for IOSs are investigated, based on which several promising application scenarios are introduced and discussed. To maximize the sum rate of an IOS-aided communication system, the authors of [22] jointly optimize the IOS configuration and the digital beamformer at the base station (BS). The proposed hybrid beamforming scheme is further validated with the aid of a hardware testbed in [25]. The authors in [26] then extend to a multi-cell IOS-aided network, where a distributed rather than centralized hybrid beamforming scheme is designed to maximize the sum rate so that no exchange of channel state information is required between the cells. The authors of [27] investigate the performance of IOS-aided non-orthogonal multiple access (NOMA) and IOS-aided orthogonal multiple access (OMA) networks, by jointly designing the IOS configuration and the resource allocation scheme. Motivated by the multiplicity of signal transformations that an RIS can apply, i.e., reflections (IRS), refractions, and joint reflections and refractions (IOS), the authors of [28]

consider an IOS-aided downlink multi-user communication network, and the corresponding system capacity is compared against that offered by surfaces that can either only reflect or refract the incident signals. In [29], the diversity gain and outage probability of an IOS-aided downlink NOMA network with randomly distributed UEs are analyzed.

The reflection-refraction models for IOSs that are employed in the existing works are, however, oversimplified, which poses some limitations on the case studies that can be analyzed and on the conclusions that can be drawn from them. Specifically, the relationship between the physical implementation of the IOS and the reflection and transmission coefficients is not explicitly given in existing research works. Therefore, the components of the IOS that can be optimized to obtain the desired reflection and refraction properties are uncertain. Besides, the existing models do not embody the impact of the angle of incidence on the reflection and transmission coefficients. As a result, the reflection and transmission coefficients employed to design the hybrid beamforming can be inaccurate, leading to system performance degradation.

The development of a circuit-based and electromagnetically consistent reflection-refraction model that embodies the aforementioned properties is, however, challenging, since the reflection and transmission coefficients are coupled. Therefore, it is challenging to construct a unified equivalent circuit-based model that accurately describes the reflection and transmission coefficients simultaneously. In this paper, we introduce a new circuit-based reflection-refraction model for a generic IOS element based on circuits theory. Based on the proposed model, in addition, we analyze the asymmetry between the reflection and transmission coefficients, and introduce a hybrid beamforming scheme to enhance the system performance. To verify the circuit-based model and to evaluate the performance of full-dimensional beamforming, we implement a prototype of IOS and deploy an IOS-assisted wireless communication testbed. Experimental measurements are conducted to quantify the performance of full-dimensional communications in terms of beam patterns and data rate. Specifically, the contributions of this paper are as follows.

- We introduce a circuit-based model for the reflection and transmission coefficients of the IOS elements. The proposed model explicitly depends on the physical structure of the IOS and on the angle of incidence of the EM waves. The EM consistency and the accuracy of the proposed model are, in addition, validated with the aid of full-wave EM simulations.
- Based on the obtained model, we analyze the asymmetry between the reflection and transmission coefficients, i.e., the reflection and transmission coefficients are shown to be different in terms of amplitude and phase responses. Besides, the proposed model is utilized

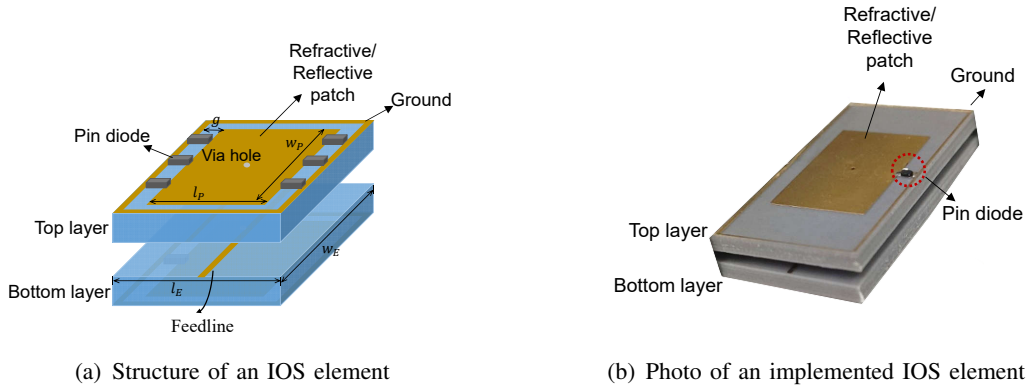


Fig. 1. Structure and one example of an IOS element.

for optimizing the hybrid beamforming of IOS-assisted networks and thus improving the system performance.

- We design and implement an IOS, and we deploy an IOS-assisted wireless communication testbed to experimentally measure the beam patterns, to quantify the achievable rate, and to verify the accuracy of the circuit-based model.

The rest of this paper is organized as follows. In Section II, we introduce the concept of IOS, we propose a new circuit-based model for the reflection and transmission coefficients for the IOS elements, and we validate the EM consistency of the model through full-wave EM simulations. In Section III, we introduce a hybrid beamforming scheme based on the proposed circuit-based model. In Section IV, we report an IOS hardware prototype, and we illustrate a testbed of an IOS-assisted wireless communication system. In Section V and Section VI, we report the adopted method for performing the measurements and the obtained experimental results, respectively. Finally, conclusions are drawn in Section VII.

II. CIRCUIT-BASED REFLECTION AND REFRACTION MODEL FOR IOSs

This section is organized as follows. The main characteristics of an IOS are introduced in Section II-A; a new circuit-based reflection and refraction model is proposed in Section II-B and is then validated with the aid of full-wave simulations in Section II-C.

A. Basics of Intelligent Omni-Surfaces

An IOS is a two-dimensional array of electrically controllable scattering elements with equal size. Each reconfigurable element consists of two symmetrical layers, and each layer contains one metallic patch and N PIN diodes that are evenly distributed on a dielectric substrate, as shown in Fig. 1. The metallic patch is connected to the ground via the PIN diodes. According to

predetermined bias voltages, the PIN diodes can be switched between their ON and OFF states, and the state of each IOS element is determined by the states of the PIN diodes on the element. At the bottom of each layer, there is a feedline that is connected to the metallic patch through a via hole. The feedline is utilized to provide the required bias voltages to the PIN diodes.

When an EM wave impinges upon the IOS element, it excites time-varying currents within the element, which reradiate the reflected and refracted EM waves. When the IOS element is configured to a different state, the surface impedance of the element changes accordingly, which in turn has an impact on the excited currents and the reradiated EM waves [30]. Therefore, the reflection and refraction properties of the IOS element depend on the state of the element, i.e., the configuration of the PIN diodes. Among all the possible states of the IOS element, N_S states are selected in order to control the EM waves. The set of selected states is denoted by \mathcal{S} . To completely characterize the reflective and refractive characteristics of the IOS, a model for the reflection and transmission coefficients is required. This is elaborated in the next subsection.

B. Circuit-based Reflection-Refraction Model

To model the reflection and refraction properties of an IOS element¹, we introduce an equivalent circuit model, as shown in Fig. 2. The proposed model has the following characteristics. The vacuum on both sides of the IOS is modeled by two semi-infinite transmission lines [31] and the IOS element is modeled as a two-port microwave network. The characteristic impedance Z_0 and the propagation constant β of the equivalent transmission line are modeled by the impedance of free space and the wave number in vacuum, respectively, i.e., $Z_0 = 377 \Omega$ and $\beta = \frac{2\pi}{\lambda}$ [32], where λ is the wavelength of the EM wave in vacuum. Since the IOS element contains four metallic layers, i.e., the metallic pattern on the top layer, the feedline on the top layer, the feedline on the bottom layer, and the metallic pattern on the bottom layer, the equivalent two-port network model consists of four metallic layers and three coupling admittances between these layers. In the following, we elaborate on these metallic layers and coupling admittances.

As illustrated in Fig. 2, each metallic layer of the IOS element is modeled with an equivalent parallel admittance that is represented by an RLC circuit. The RLC equivalent circuit for the metallic pattern consists of two capacitors, two inductors, one resistor, and several PIN diodes.

¹The main objective of this paper is to characterize the impact of the IOS physical structure and the angle of incidence on the reflection and transmission coefficients. Therefore, we do not consider the effect of polarization, and assume that the incident signal is a transverse electric (TE) polarized wave as a case study.

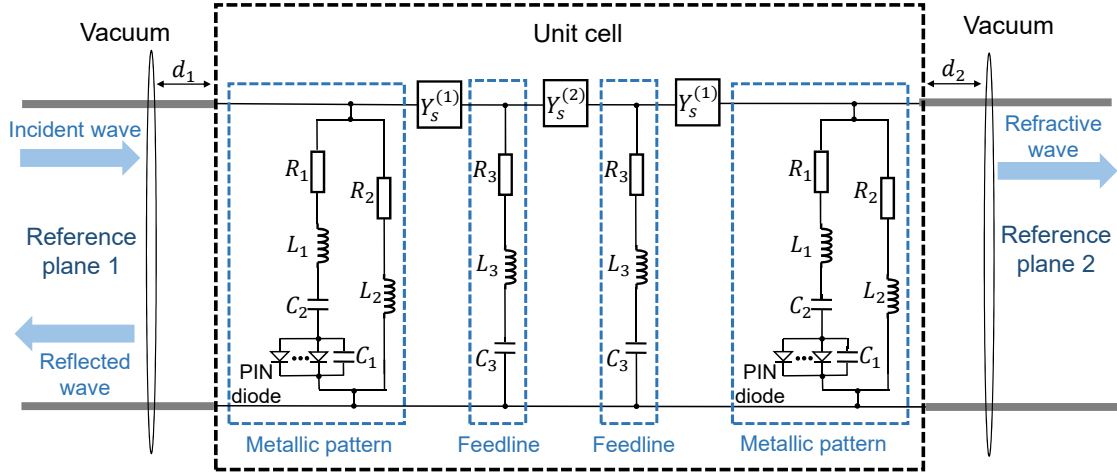


Fig. 2. Equivalent circuit model of the IOS element.

Specifically, C_1 and C_2 describe the capacitances formed by the patch and the ground. Both C_1 and C_2 are positively correlated with the width w_E of the IOS element and with the width w_P of the metallic patch, and they are negatively correlated with the gap g between the patch and the ground [33]. The parameters L_1 and R_1 represent the inductance and the resistance of the central metallic patch, respectively, where the inductance L_1 increases with the length l_P of the patch [33]. Moreover, L_2 and R_2 model the inductance and resistance generated by the ground, respectively, where L_2 is positively correlated with the length l_E of the ground. Each PIN diode can be modeled with an equivalent RLC circuit as well, whose structure depends on the state of the PIN diode [34]. The RLC equivalent circuit of the feedline is constituted by the series of the resistance R_3 , the inductance L_3 , and the capacitance C_3 , where R_3 and L_3 are generated by the feedline while the capacitance C_3 is formed by the feedline of the IOS element and the feedline of the neighbouring element. Specifically, the capacitance C_3 increases with the length w_E of the feedline and decreases with the length l_E of the element. Also, the larger the width w_F of the feedline, the larger the inductance L_3 . The coupling effects between adjacent metallic layers can be described by coupling admittances. Since the IOS consists of two symmetric layers, the coupling admittance between the metallic pattern and the feedline on the top layer is the same as that between the metallic pattern and the feedline on the bottom layer. These admittances are represented by $Y_S^{(1)}$. Besides, $Y_S^{(2)}$ is the coupling admittance between the feedline on the top layer and the feedline on the bottom layer.

Based on the equivalent two-port network illustrated in Fig. 2, the ABCD transmission matrix

of the obtained network can be expressed as [35]

$$\begin{bmatrix} A & B \\ C & D \end{bmatrix} = \begin{bmatrix} 1 & 0 \\ Y_P^{U,M} & 1 \end{bmatrix} \begin{bmatrix} 1 & \frac{1}{Y_s^{(1)}} \\ 0 & 1 \end{bmatrix} \begin{bmatrix} 1 & 0 \\ Y_P^{U,F} & 1 \end{bmatrix} \begin{bmatrix} 1 & \frac{1}{Y_s^{(2)}} \\ 0 & 1 \end{bmatrix} \begin{bmatrix} 1 & 0 \\ Y_P^{L,F} & 1 \end{bmatrix} \begin{bmatrix} 1 & \frac{1}{Y_s^{(1)}} \\ 0 & 1 \end{bmatrix} \begin{bmatrix} 1 & 0 \\ Y_P^{L,M} & 1 \end{bmatrix}, \quad (1)$$

where $Y_P^{U,M}$, $Y_P^{U,F}$, $Y_P^{L,F}$, and $Y_P^{L,M}$ denote the parallel admittances that correspond to the metallic pattern on the top layer, the feedline on the top layer, the feedline on the bottom layer, and the metallic pattern on the bottom layer, respectively. These admittances can be expressed as

$$Y_P^{U,M} = \left(R_1 + j\omega L_1 + (j\omega C_2)^{-1} + \left(\sum_{i \in \mathcal{U}} Y_{pin}^i + j\omega C_1 \right)^{-1} \right)^{-1} + (R_2 + j\omega L_2)^{-1}, \quad (2)$$

$$Y_P^{U,F} = Y_P^{L,F} = (R_3 + j\omega L_3 + (j\omega C_3)^{-1})^{-1}, \quad (3)$$

$$Y_P^{L,M} = \left(R_1 + j\omega L_1 + (j\omega C_2)^{-1} + \left(\sum_{i \in \mathcal{L}} Y_{pin}^i + j\omega C_1 \right)^{-1} \right)^{-1} + (R_2 + j\omega L_2)^{-1}, \quad (4)$$

respectively, where ω is the angular frequency, Y_{pin}^i denotes the admittance of the i -th PIN diode, which is determined by the state of the PIN diode, and \mathcal{U} and \mathcal{L} represent the set of PIN diodes on the upper and lower metallic layers of the IOS element, respectively.

Based on the ABCD transmission matrix in (1), the reflection and transmission coefficients of the considered IOS element can be formulated as [31, Table 4.2]

$$\Gamma_r = \frac{(A + B/Z_0) - Z_0(C + D/Z_0)}{(A + B/Z_0) + Z_0(C + D/Z_0)} \exp(-j2\beta d_1), \quad (5)$$

and

$$\Gamma_t = \frac{2}{(A + B/Z_0) + Z_0(C + D/Z_0)} \exp(-j\beta(d_1 + d_2)), \quad (6)$$

respectively, where d_1 and d_2 represent the distances between the reference planes and the surface of the IOS element. The terms $\exp(-j2\beta d_1)$ in (5) and $\exp(-j\beta(d_1 + d_2))$ in (6) account for the distances with respect to the IOS at which the reflection and transmission coefficients are measured, e.g., when analyzing the IOS element with the aid of full-wave EM simulations. Therefore, d_1 and d_2 are fixed throughout this paper, and they cannot be designed to optimize the reflection and transmission coefficients. The reflection-refraction model for the IOS proposed in (5) and (6) depends on the specific circuitual implementation of the IOS element and the tuning circuits, i.e., the PIN diodes. Therefore, it offers a realistic and accurate model for wireless applications. As far as (1), (5), and (6) are concerned, three remarks are in order.

Remark 1. *The IOS cannot be configured to operate as a purely reflecting surface, i.e., we always have $|\Gamma_t| \neq 0$. If, however, we ensure that $|(A + B/Z_0) + Z_0(C + D/Z_0)|$ is sufficiently*

large, the refracted power can be made small.

On the contrary, a purely refracting IOS element is obtained by setting $(A + B/Z_0) = Z_0(C + D/Z_0)$. In this case, the reflection and transmission coefficients in (5) and (6) reduce to $\Gamma_r = 0$ and $\Gamma_t = (A + B/Z_0)^{-1} \exp(-j\beta(d_1 + d_2))$, respectively.

Remark 2. It is worth noting that the ABCD transmission matrix in (1), and the reflection and transmission coefficients in (5) and (6), respectively, are derived under the so-called **locally periodic boundary condition** [13]. In other words, we consider an IOS element whose equivalent circuit is given in Fig. 2, in which the PIN diodes are set to a given state. Then, we construct a continuous, infinitely large, and homogeneous surface, where the equivalent circuit-based model of the considered IOS element applies to every single point (unit cell) of the surface. The reflection and transmission coefficients in (5) and (6) correspond to this locally equivalent system, in which the incident EM waves are reflected and refracted specularly, i.e., the angles of reflection and refraction coincide with the angle of incidence.

It is worth mentioning that the equivalent circuit parameters in (1) are determined by projected geometric parameters of the unit cell [33]. Therefore, the equivalent circuit parameters depend on the angle of incidence, i.e., the inductances, capacitances, resistances, and coupling admittances can be formally written as $(L_1(\theta, \phi), L_2(\theta, \phi), L_3(\theta, \phi))$, $(C_1(\theta, \phi), C_2(\theta, \phi), C_3(\theta, \phi))$, $(R_1(\theta, \phi), R_2(\theta, \phi), R_3(\theta, \phi))$, $(Y_s^{(1)}(\theta, \phi), Y_s^{(2)}(\theta, \phi))$, respectively, where (θ, ϕ) is the angle of incidence. For ease of writing, the angle of incidence (θ, ϕ) is not explicitly stated in (1) and in the subsequent equations. By taking into account the angle-dependence of the equivalent circuit parameters, we can derive the following remark.

Remark 3. The reflection and transmission coefficients in (5) and (6) depend on the angle of incidence². Since the proposed reflection-refraction model is based on the locally periodic boundary condition, the angle of reflection of the locally-periodic equivalent of the IOS element is equal to the angle of incidence and, therefore, its dependence is implicitly considered. Thanks to Huygens's principle, however, the whole IOS is capable of realizing anomalous reflections and refractions by adjusting the local reflection coefficient of the IOS elements.

Besides, the reflection and transmission coefficients depend on the geometric structure of the IOS element, i.e., the geometric period $w_E \times l_E$ of the IOS array, the size $w_M \times l_M$ of the metallic patch, the gap g between the ground and the metallic patch, and the width w_F of the feedline.

²For a purely refracting element, the transmission coefficient depends on the angle of incidence of the EM wave.

Compared to existing reflection-refraction models, either for IRSs or IOSs (see, e.g., [13], Table I), the proposed reflection-refraction model explicitly depends on the hardware implementation of the IOS element, it is electromagnetically consistent under the locally periodic boundary condition, and it allows us to formulate optimization problems in wireless communications that explicitly depend on the tuning circuits for a given geometric structure of the IOS element. The importance of utilizing accurate scattering models for reconfigurable surfaces has recently been analyzed in [36] with the aid of simulations.

C. Full-wave Validation of the Proposed Circuit-based Reflection-Refraction Model

As mentioned in the previous section, the proposed circuit-based reflection-refraction model of the IOS element depends on a large number of parameters and is derived under the assumption of locally periodic boundary condition. In this section, we aim to validate the proposed model with the aid of full-wave EM simulations. To this end, we consider an implementation of the IOS element, and compare the reflection and transmission coefficients in (5) and (6) against those obtained by using a full-wave simulator, i.e., without relying on the circuit-based model in Fig. 2 but numerically solving Maxwell's equations.

Specifically, we consider an IOS element that operates at 3.6 GHz and assume that the tunability is ensured by one PIN diode located in the upper metallic plate and by one PIN diode located in the lower metallic plate. The size of the sample IOS element is $2.87 \times 1.42 \times 0.71$ cm³, which implies that the largest side of the IOS element is approximately one-third of the wavelength at 3.6 GHz. The two layers that constitute the IOS element are separated by a distance of 0.3 cm. On each layer, a rectangular copper patch whose size is 1.6×1.0 cm² (i.e., the size of the patch is approximately $\lambda/5.21 \times \lambda/8.33$ with $\lambda \approx 8.33$ cm at 3.6 GHz) is printed on a dielectric woven-glass PTFE substrate with permittivity $\epsilon = 2.2$ and loss tangent $0.0019@3.6$ GHz. The copper feedline on the other side of the substrate has width equal to 0.04 cm, and the thickness of the patch and the feedline are 3.9×10^{-3} cm. On the boundary of each layer, there is the ground whose width is 0.02 cm. The ground is connected to the patch through a BAR 65-02L PIN diode. The equivalent circuit model of the PIN diode is presented in Fig. 3 for completeness [34]. In the considered example, each IOS element is assumed to be reconfigurable according to two states: both PIN diodes are set to the ON state, i.e., the state (ON, ON), and both diodes are set to the OFF state, i.e., the state (OFF, OFF). Therefore, the set \mathcal{S} has two elements, i.e., $N_{\mathcal{S}} = 2$.

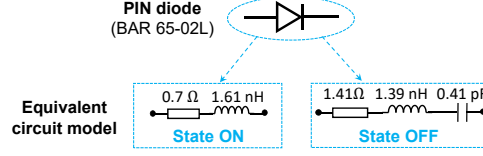


Fig. 3. Equivalent circuit model of the PIN diode.

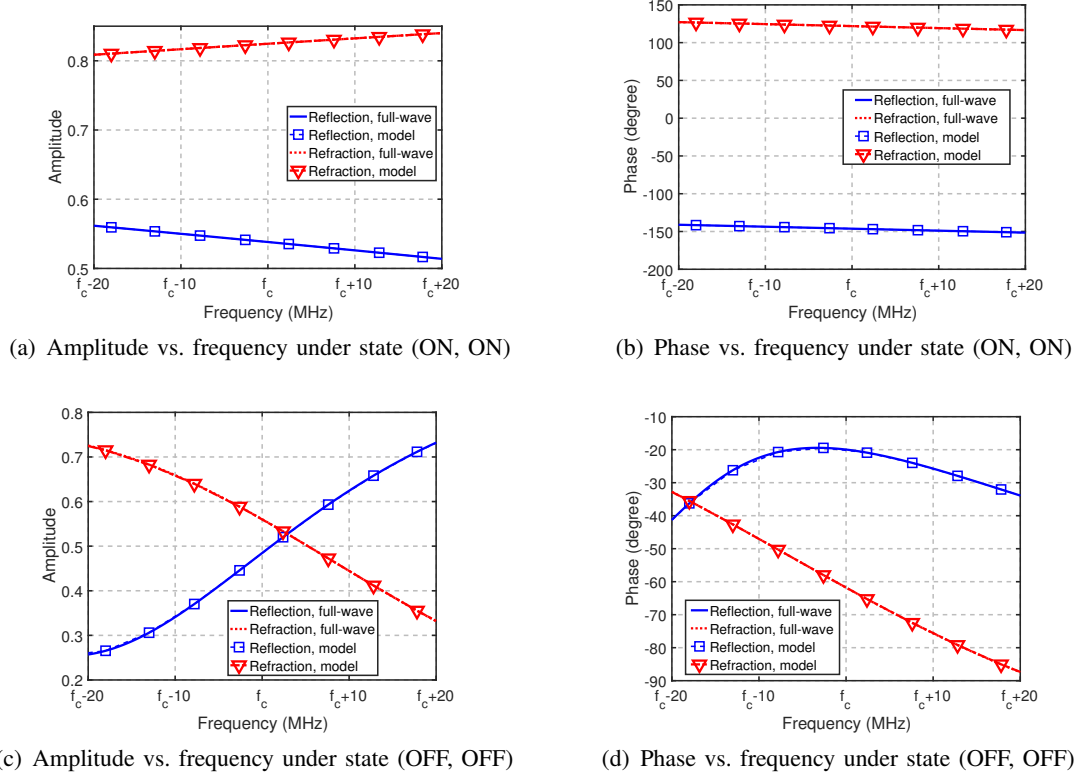


Fig. 4. Amplitude and phase responses of the IOS element versus the operating frequency under normal incidence. Comparison between full-wave simulations and the proposed model. The center frequency is $f_c = 3.6$ GHz.

The full-wave EM simulations are performed by using Microwave Studio and the Transient Simulation Package in the CST software. In the simulations, we assume a plane wave that impinges normally on the IOS element. The EM characterization of the IOS element is performed by imposing the locally periodic boundary condition with Floquet's ports. The distances between the reference planes of the Floquet's ports and the surfaces of the IOS element are $d_1 = d_2 = 0.84\lambda$. In addition, the equivalent circuit model of the PIN diodes is input into the simulation software [37]. The comparison between the full-wave simulations and the proposed circuit-based model is reported in Fig. 4. *The obtained results show that the proposed model provides a good accuracy for the considered case study.* Specifically, the curves of the circuit-based model are obtained by using (5) and (6) with the circuit parameters reported in Table I and Fig. 5. These parameters are obtained by matching, through curve fitting, the analytical expressions of the

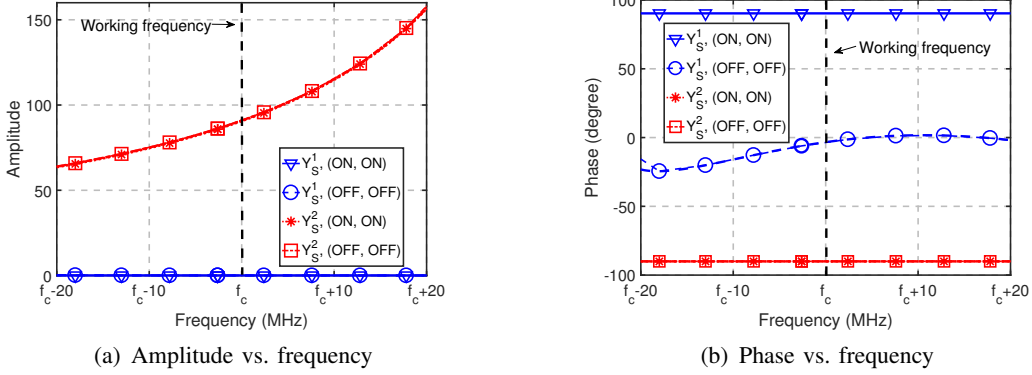


Fig. 5. The interlayer coupling admittances $Y_s^{(1)}$ and $Y_s^{(2)}$ of the IOS element under normal incidence. The center frequency is $f_c = 3.6$ GHz. $Y_s^{(1)}$ and $Y_s^{(2)}$ depend on the frequency of operation.

TABLE I. Equivalent circuit parameters of the IOS element under normal incidence

Parameter	R_1 (Ω)	R_2 (Ω)	R_3 (Ω)	L_1 (nH)	L_2 (nH)	L_3 (nH)	C_1 (pF)	C_2 (pF)	C_3 (pF)
Value	$10^{-3.18}$	$10^{-3.78}$	$10^{-7.07}$	$10^{-3.17}$	0.40	$10^{-2.04}$	8.03	962.24	209.45

reflection and transmission coefficients in (5) and (6) with those obtained from the full-wave EM simulations with CST. The corresponding fitting problem is a quadratic program that is solved by using standard optimization tools. The solution reported in Table I and Fig. 5 is, of course, not unique. However, this approach substantiates the analytical circuit-based model in (1), (5), and (6). As mentioned in previous text, the parameters in Table I and Fig. 5 are expected to be different under oblique incidence, and the corresponding circuit parameters can be found by using a similar approach.

By direct inspection of Fig. 4, the following observations can be made:

- Fig. 4(c) indicates that only 55% of the incident EM power is reflected and refracted by the IOS element under state (OFF, OFF), i.e., $|\Gamma_r|^2 + |\Gamma_t|^2 = 0.55$ under state (OFF, OFF). This is mainly due to the severe losses in the substrate. These losses can be reduced by utilizing a different substrate with a smaller loss tangent and by modifying the geometric structure of the IOS element so that its resonant frequency is significantly different from the working frequency.
- By comparing Fig. 4(b) and Fig. 4(d), at the center frequency f_c , we see that the phase difference between the two states of the IOS element is approximately 180° for the refracted signal but only approximately 130° for the reflected signal. The reason is that the difference of the resonant frequency between the two states of the IOS is not large enough.
- From Fig. 4, we find that the reflection and refraction responses can be different in terms of

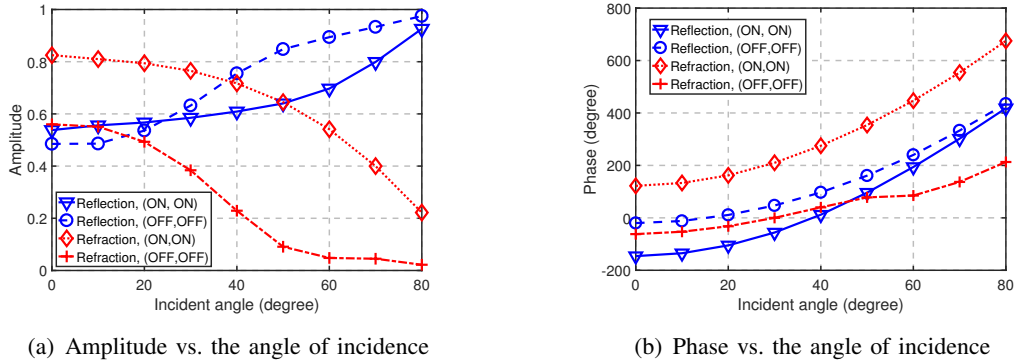


Fig. 6. Full-wave simulations of the reflection and transmission coefficients vs. the angle of incidence. The operating frequency is 3.6 GHz.

amplitude and phase shift, as dictated by (5) and (6). According to (5) and (6), specifically, this implies that the power ratio and the phase shift difference between the reflected and refracted signals are determined by the geometric structure and hardware implementation of the IOS element. The current implementation of the IOS element does not allow us to adjust the power ratio and the phase shift difference between the reflected and refracted signals. The design of a reconfigurable IOS element with these tunable characteristics is postponed to a future implementation.

As mentioned in Remark 3, the reflection and transmission coefficients in (5) and (6) depend on the angle of incidence of the EM waves. This remark is validated in Fig. 6 with the aid of full-wave EM simulations. Figure 6 confirms that the reflection and transmission coefficients depend on the angle of incidence. Also, the angle-dependence is different for the (ON, ON) and (OFF, OFF) states. Specifically, the following observations can be made from Fig. 6:

- From Fig. 6(a), we see that the amplitude of the reflection and transmission coefficients increases and decreases, respectively, with the angle of incidence. This implies that, in general, the amount of power that is reflected and refracted depends on the angle of incidence.
- From Fig. 6(b), we see that the designed IOS element offers, however, better performance in refraction than in reflection. The reason is that the phase difference between the two states of the IOS element is approximately equal to 180° for the refracted wave, while it tends to shrink for the reflected wave as the angle of incidence increases. This implies that, for the reflected waves, it is not possible to impose the required phase shift on the waves that impinge on the IOS from a wide angle of incidence. Good reflection capabilities are

obtained for angles of incidence that are less than 40° .

III. FULL-DIMENSIONAL BEAMFORMING

Based on the proposed reflection-refraction model, we introduce in Section III-A a general framework for hybrid beamforming, which is specifically tailored for full-dimensional communications. In Section III-B, we then introduce different performance metrics for optimizing and evaluating full-dimensional communications.

A. General Framework for Hybrid Beamforming

We first introduce the basic concepts for hybrid beamforming. In an IOS-assisted network, the BS and the IOS perform *digital beamforming* and *analog beamforming*, respectively. Specifically, the BS first encodes multiple data streams via a digital beamformer \mathbf{V}_D . Then, the encoded signal is up-converted to the desired carrier frequency and is transmitted through K_t transmit antennas. When the signals from the BS impinge upon the IOS, each IOS element reflects and refracts the incident signal by applying a certain phase shift to the signal. This operation is referred to as analog beamforming, and it is usually realized through a wireless control channel that the BS utilizes to configure the amplitude and phase responses of the IOS elements. Reconfigurable surfaces that do not need any control channels have recently been proposed as well, but they are out of the scope of this paper [38]. In full-dimensional communications, therefore, the digital beamformer at the BS and the analog beamformer at the IOS can be jointly optimized for achieving the optimal performance.

At the first sight, this hybrid beamforming design is similar to IRS-assisted communications. However, IOS-aided systems face several new design challenges. First, the reflection and transmission coefficients of the IOS can be asymmetric, which implies that the channel models of the UEs on two sides of the IOS are in general different. Therefore, the hybrid beamforming schemes utilized for IRSs cannot be directly applied to IOSs. Second, differently from an IRS, an IOS is deployed to support full-dimensional communications on both sides of the surface. Therefore, the design of the hybrid beamforming needs to account for both the reflection and transmission coefficients, and the coverage or rate requirements on both sides of the surface.

To cope with these design challenges, we formulate a joint BS digital beamforming and IOS analog beamforming optimization problem. Let $G(\mathbf{V}_D, \mathbf{s})$ denote the generic performance metric of interest (to be detailed in the next section), where \mathbf{V}_D and \mathbf{s} denote the BS digital beamforming

matrix and the IOS analog beamforming vector, respectively³. Specifically, the state of the m -th IOS element is denoted by s_m . Also, the reflection and transmission coefficients of the m -th IOS element when the signal transmitted by the k -th Tx antenna impinges upon the element are represented by $\Gamma_r^{m,k}$ and $\Gamma_t^{m,k}$, respectively, and the angle of incidence is denoted by $(\theta_{in}^{m,k}, \phi_{in}^{m,k})$.

Then, the optimization problem can be formulated as

$$\max_{\mathbf{V}_D, \mathbf{s}} G(\mathbf{V}_D, \mathbf{s}), \quad (7a)$$

$$s.t. \gamma_j \geq \gamma_0, \quad (7b)$$

$$[\mathbf{V}_D \mathbf{V}_D^H]_{k,k} \leq P_T, \quad (7c)$$

$$(\Gamma_r^{m,k}, \Gamma_t^{m,k}) \in \left\{ \left(\Gamma_r(\theta_{in}^{m,k}, \phi_{in}^{m,k}, s_m), \Gamma_t(\theta_{in}^{m,k}, \phi_{in}^{m,k}, s_m) \right) \right\}_{s_m \in \mathcal{S}}, \forall m, \quad (7d)$$

where the constraint in (7b) ensures the desired quality of service for each UE by making sure that the received signal-to-interference-and-noise ratio γ_j is larger than a predetermined threshold γ_0 , the constraint in (7c) ensures that the transmit power of each antenna at the BS cannot exceed the maximum value P_T , and the constraint in (7d) indicates that the reflection and transmission coefficients of the m -th IOS element can only take discrete values that belong to the finite set \mathcal{S} . It is worthwhile noting that the constraint in (7d) depends on the angle of incidence. Specifically, the reflection and transmission coefficients of each IOS element belong to a different feasible set because the angle of incidence is not usually the same for all the IOS elements. Only when the transmitter is in the far-field of the IOS, the curvature of the incident wave across the surface of the IOS can be ignored, and the angle of incidence can be assumed to be the same across the entire IOS. Efficient algorithms to solve the problem in (7) can be found in [25] and [39]. Specifically, for computational efficiency, the digital beamformer and the IOS configuration are optimized alternatively. For the digital beamforming subproblem, the channels are fixed because the IOS configuration is given. Therefore, the problem is a well-known digital beamforming problem, and thus the zero-forcing digital beamformer is adopted to obtain a near optimal solution [40]. For the analog beamforming subproblem, the states of the IOS elements are optimized one-by-one to further reduce the computational complexity, i.e., one at a time, the state of only one IOS element is optimized to maximize the system performance in (7a) given the states of the other IOS elements.

³The general function $G(\mathbf{V}_D, \mathbf{s})$ can be any performance metric mentioned in Section III-B.

B. Performance Metrics

In this section, we summarize relevant performance metrics that can be considered for optimizing full-dimensional communications. These performance metrics correspond to the objective function in (7a). The considered performance metrics are divided into two categories: *beam pattern related* and *data rate related*.

1) *Beam pattern related metrics*: We focus our attention on the beam pattern corresponding to the j -th UE, which refers to the normalized power that is scattered by the IOS as a function of a generic direction of observation under the assumption that the IOS is optimized for maximizing the power towards the location of the j -th UE. Four metrics related to the optimization of the beam pattern are considered.

- **Beam direction**: The direction of a beam is defined as the direction of the main lobe.
- **Half-power beamwidth (HPBW)**: The HPBW identifies the range of directions towards which the radiated power is no smaller than half of the power radiated towards the beam direction [41]. A narrower beamwidth indicates a larger beamforming gain, which can lead to a stronger desired signal. Also, a narrow beamwidth reduces the inter-user interference among closely-spaced UEs.
- **Sidelobe level (SLL)**: The SLL refers to the power difference of the largest sidelobe with respect to the main lobe [42]. The SLL is an effective metric to quantify the amount of interference generated towards undesired directions. The smaller the SLL, the smaller the interference.
- **Scattering efficiency**: The scattering efficiency is defined as the percentage of power in the main beam with respect to the total scattered power [43]. The larger the scattering efficiency, the stronger the desired signal and the smaller the interference.

Therefore, a well designed IOS is characterized by a narrow HPBW, a low SLL, and a high scattering efficiency, while steering the beams towards the desired UEs. In an IOS, this needs to be jointly ensured for the reflected and refracted beams. Specifically, the beam pattern of an IOS is directly determined by the reflection and transmission coefficients in (5) and (6), respectively, and the digital beamforming matrix \mathbf{V}_D . In mathematical terms, the beam pattern corresponding to the j -th UE can be formulated as

$$F_j(\theta, \phi) = \left| \sum_k E_k(\theta, \phi) V_{D_{k,j}} \right|^2, \quad (8)$$

where (θ, ϕ) is the far-field angle under which the IOS views the j -th UE, $V_{D_{k,j}}$ is the k -th element in the j -th row of the digital beamforming matrix \mathbf{V}_D at the BS, and $E_k(\theta, \phi)$ is the electric field scattered by the IOS towards the direction (θ, ϕ) under the assumption that only the k -th antenna of the BS is activated. Specifically, $E_k(\theta, \phi)$ is determined by the configuration of the IOS, i.e., by the reflection and transmission coefficients in (5) and (6), and it is independent of the BS digital beamformer. In the following, $E_k(\theta, \phi)$ is referred to as the *reference beam pattern*. The proposed model in (8) is validated through experimental results in Appendix A.

2) *Data rate*: The data rate is a typical performance metric of interest in wireless communications. In a multi-user scenario, it is defined as the sum-rate over all the UEs. Specifically, the data rate of j -th UE is defined as [22]

$$R_j = \log_2 \left(1 + \frac{\left| C_j \sum_k V_{D_{k,j}} h_{k,j} \right|^2}{\sigma^2 + \sum_{j' \neq j} \left| C_j \sum_k V_{D_{k,j'}} h_{k,j'} \right|^2} \right). \quad (9)$$

where C_j accounts for the joint impact of the RF chains at the BS and the j -th UE, σ^2 is the variance of the zero-mean additive white Gaussian noise (AWGN) at the j -th UE, and $h_{k,j}$ is the channel gain from the k -th antenna of the BS to the j -th UE, which includes the impact of the IOS. As far as the IOS is concerned, we consider the same model as in [28]. More precisely, we assume that the IOS elements are partitioned into M groups and that the elements belonging to the same group are set to the same state⁴. This is a typical approach for realizing reconfigurable surfaces at a reduced complexity. Then, the IOS-aided channel $h_{k,j}$ can be formulated as [44]

$$h_{k,j} = h_{k,j}(s_1 = 0, \dots, s_M = 0) + \sum_{m=1}^M s_m \Delta h_{k,j}^{(m)}, \quad (10)$$

where s_m denotes the state of the m -th group of IOS elements, $\Delta h_{k,j}^{(m)}$ denotes the channel difference when s_m changes from the state 0, i.e., the (OFF, OFF) state, to the state 1, i.e., the (ON, ON) state, and the other groups of IOS elements are kept to the state 0. In mathematical terms, we have

$$\Delta h_{k,j}^{(m)} = h_{k,j}(s_1 = 0, \dots, s_m = 1, \dots, s_M = 0) - h_{k,j}(s_1 = 0, \dots, s_M = 0). \quad (11)$$

⁴In general, the grouping strategy needs to jointly consider the system performance and the implementation complexity, which can be broadly summarized as follows: 1) Grouping adjacent IOS elements rather than dispersed elements is beneficial to simplify the design of the feedline network, especially if each group contains the same number of elements; 2) Minimizing the number of groups while fulfilling the required system performance, so as to find a desirable tradeoff between system performance and implementation complexity.

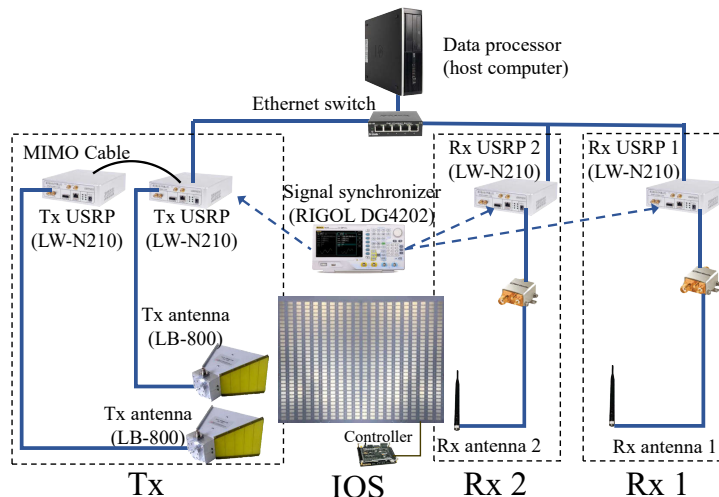


Fig. 7. Hardware modules of the implemented IOS prototype.

IV. EXPERIMENTAL PROTOTYPE

In order to experimentally validate the proposed reflection-refraction model for the IOS, and to evaluate the performance of full-dimensional beamforming, we realized an IOS hardware prototype that is described in this section.

A. Implementation of the IOS

As shown in Fig. 7, the implemented IOS consists of 640 reconfigurable elements. The structure and the electromagnetic characterization of each IOS element was introduced in Section II-C. To configure the states of the IOS elements in order to manipulate the incident waves, we utilize a field-programmable gate array (FPGA) platform that mimics the function of the IOS controller. A software program is pre-loaded in the FPGA, and the states of the IOS elements are changed automatically by controlling the FPGA. The FPGA is a Cyclone IV EP4CE10F17C8 platform that is manufactured by Intel Altera corporation. The development board that contains the FPGA and various interfaces is manufactured by ALINX. The hardware description language used for programming the FPGA is Verilog.

B. Hardware Modules of the Prototype

As shown in Fig. 7, the developed IOS hardware platform comprises the following modules.

- *Transmitter*: The transmitter (Tx) includes two transmit elements. Each transmit element is constituted by a universal software radio peripheral (USRP) platform. Specifically, an LW N210 USRP platform with an SBX-LW120 RF daughterboard is used. The output port of each USRP is connected to a directional double-ridged horn antenna whose gain is 12.5 dBi at the working frequency of 3.6 GHz. The antenna is manufactured by A-INFO

Corporation and the part number is LB-880. A MIMO cable is utilized to synchronize the transmission of data between the two USRP platforms. Each USRP platform implements the carrier modulation⁵, power amplification, and filtering by using a GNU radio software development kit [45]. The maximum transmit power is 20 dBm.

- *Receiver:* Two receivers (Rxs) are implemented. Each receive element is constituted by one USRP, one low-noise amplifier (LNA), and one cylindrical antenna. The signal received by the antenna is first amplified by the LNA whose part number is ZX60-43-S+, and it is then sent to the USRP for the carrier demodulation and the baseband processing. The gain of the antenna and the gain of the LNA are 3 dBi and 15.07 dB, respectively, at 3.6 GHz.
- *Signal synchronizer:* To accurately detect the relative phases of the received signals with respect to the transmitted signals, a clock source that outputs the same clock signal to the Tx USRP and Rx USRPs is utilized, and a RIGOL DG4202 signal source generator is used to generate the same pulse-per-second (pps) signal to the USRPs. The synchronization of the clock and pps signals can reduce the time-variance of the carrier phase difference between the Tx and Rx USRPs, which improves the accuracy for measuring the channel phase⁶.
- *Ethernet switch:* The Ethernet switch connects the transmitter and the receivers to a host computer to exchange information. Specifically, through the Ethernet switch, the host computer sends the control signals to the transmitter and receiver units, and the receivers return their received signals to the host computer. The bandwidth of the switch is about 1 GHz.
- *Data processor:* The data processor is a host computer that controls the transmitter and the receivers through a software program written in Python. The digital beamforming is operated by the data processor as well.

As a whole, the different modules of the IOS prototype (in particular the USRP and the FPGA) are coordinated through a software program written in Python that runs on the host computer. Specifically, the host computer configures the USRP platforms through the GNU Radio software development kit. The FPGA, in turn, transforms the input from the host computer into a control signal for the IOS with the aid of a software program written in Verilog.

⁵The implemented IOS-based prototype does not perform digital modulation and coding, since we evaluate the theoretical rate in (9).

⁶Fig. 7 illustrates an indoor application where Rx 1 and Rx 2 on two sides of the IOS are synchronized with the Tx.

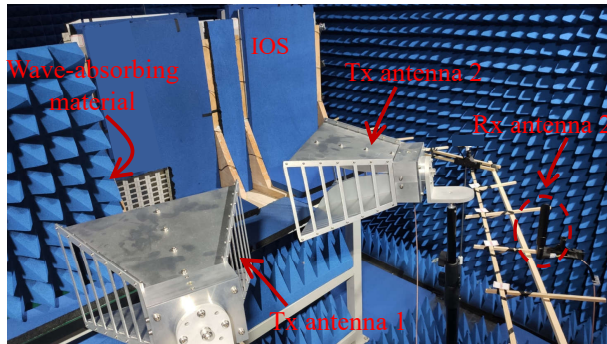


Fig. 8. Environment for measuring the beam patterns.

V. MEASUREMENT PROCEDURES

In this section, we introduce the measurement procedures that are utilized to characterize the beam pattern (Section V-A) and the data rate (Section V-B).

A. Beam Pattern

In order to experimentally evaluate the performance of the IOS in terms of reradiation capabilities, the beam pattern of a generic UE in (8) needs to be first measured and then analyzed in terms of different performance metrics. To this end, the reference beam patterns that characterize the IOS as a function of its configuration need to be measured. In this section, we describe, without loss of generality, the procedure for measuring the reference beam pattern that corresponds to the receiver Rx 1 in Fig. 7.

To measure the reference beam patterns for different IOS configurations, we deploy the transmitter, the receiver, and the IOS as illustrated in Fig. 8. Since we consider the receiver Rx 1, the transmitter is configured so that the symbols x_2 intended for Rx 2 is set equal to zero, i.e., $x_2 = 0$, in order to avoid interference. For simplicity of measurement, the transmitted signal x_1 intended for Rx 1 is set equal to $x_1 = 1$, i.e., a sequence of all ones is transmitted to Rx 1. By definition, as mentioned, the reference beam pattern $E_k(\theta, \phi)$ is obtained by turning the k -th transmit antenna on and by turning all the other transmit antennas off.

To conduct the measurements, we carefully setup the measurement environment as illustrated in Fig. 8. The IOS prototype is deployed within a room whose walls are made of aluminum in order to block environmental EM interference. To avoid environmental scatterings, the wall of the room is covered with wave absorbing material. To measure only the beam scattered by the IOS, the direct link between the transmitter and the receiver needs to be strongly attenuated. To this end, the transmitter is placed closer to the IOS as compared to the distance between the Rx and the IOS, and some wave-absorbing material is placed in the middle of the room. To measure

the reradiation pattern of the IOS as a function of the angle of observation, we build a circular measurement platform that is located parallel to the ground⁷. Then, the reference field pattern $E_k(\theta, \phi)$ is measured by deploying Rx 1 in different locations on the measurement platform. Once the reference beam patterns are measured, the beam pattern of the IOS is obtained from (8), where the BS digital beamforming matrix in (8) is determined by utilizing the algorithm described in Section III-A.

B. Data Rate

In order to measure the data rate, we utilize the following approach. First, we measure the channel parameters, and then we insert them in (9)-(11) for obtaining the data rate. This procedure is convenient because the acquisition of the channel parameters is needed for optimizing the IOS configuration and the BS digital beamforming matrix.

Based on (9)-(11), the estimation of $C_j h_{k,j}$ is sufficient to compute the rate⁸. Specifically, $C_j h_{k,j}$ are extracted by setting the IOS to a specific configuration and by measuring the received signal. Let k and k' denote the indices of the two transmit antennas in Fig. 7, and let j' denote the index of the Rx other than Rx j . Then, the signal received at the j -th receiver (i.e., Rx j) can be expressed as [46]

$$y_j = C_j V_{D_{k,j}} h_{k,j} x_j + C_j V_{D_{k',j}} h_{k',j} x_{j'} + C_j \sum_{k_t \in \{k, k'\}} V_{D_{k_t, j'}} h_{k_t, j'} x_{j'} + n_j \quad (12)$$

where x_j and $x_{j'}$ denote the intended signal for Rx j and Rx j' , respectively, and n_j is the receive AWGN. The first two terms on the right-hand side of (12) represent the desired signals from the k -th and the k' -th antennas of the transmitter, respectively. On the other hand, the third term denotes the inter-user interference. Based on (12), the channel parameter $C_j h_{k,j}$ are acquired by extracting the first term from the received signal y_j , and by dividing it by $x_j V_{D_{k,j}}$. To this end, the inter-user interference $C_j \sum_{k_t \in \{k, k'\}} V_{D_{k_t, j'}} h_{k_t, j'} x_{j'}$ needs to be mitigated by setting $\{V_{D_{k, j'}}, V_{D_{k', j'}}\} = 0$, and the signal $C_j V_{D_{k', j}} h_{k', j}$ needs to be mitigated by setting $V_{D_{k', j}} = 0$. The impact of the AWGN n_j is weakened by increasing the gain C_j of the RF chains, so as to enhance the signal-to-noise-ratio.

To estimate the rate in (9), the variance σ^2 of the received AWGN is necessary as well. To measure the variance σ^2 , the transmitter is turned off and the unbiased estimator $\sum_{u=1}^U (y_u -$

⁷For simplicity of measurement, we focus our attention on the beam within the horizontal plane instead of the three-dimensional beam pattern. Therefore, a measurement platform parallel to ground is sufficient.

⁸The implemented IOS-based prototype does not perform signal detection, since we evaluate the theoretical rate in (9).

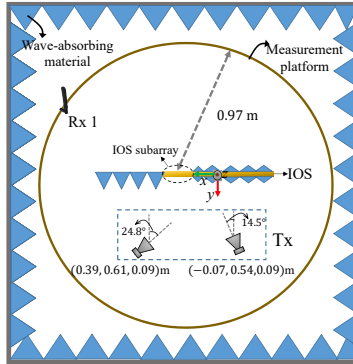


Fig. 9. Experimental layout for measuring the beam patterns.

$\bar{y})^2/(U - 1)$ is utilized [47], where y_u is one sample of (12), and \bar{y} is the average values from U collected samples. Once the channel parameters and the noise variance are obtained, the data rate in (9) is computed by setting the configuration of the BS according to the hybrid beamforming algorithm formulated in Section III-A.

VI. EXPERIMENTAL RESULTS

In this section, we describe experimental results obtained with the implemented IOS prototype, as well as we evaluate the performance of full-dimensional beamforming and verify the theoretical findings.

A. Analysis of the Beam Pattern

As mentioned, we analyze the beam pattern that corresponds to the receiver Rx 1. Since the size of the room is not large enough to measure the far-field beam pattern of the whole IOS, the experiments are conducted by considering a portion of the IOS (subarray), which consists of 8 rows and 5 columns of IOS elements, whose total size is $14.35 \times 11.36 \times 0.71 \text{ cm}^3$. To simplify the configuration of the IOS subarray, it is split into 8 groups. Each group comprises one row of IOS elements, and the IOS elements within one group are set to the same state. To avoid undesired scattering, in addition, the rest of the IOS is covered with wave absorbing material, as shown in Fig. 8. Therefore, the circular measurement platform is centered in correspondence of the IOS subarray, as shown in Fig. 9. The locations and orientations of the transmit and receive antennas are illustrated in Fig. 9 as well. In particular, the observation distance with respect to the center of the IOS subarray is 0.97 m. This implies that the observation points are in the Fraunhofer far-field distance of the IOS subarray, which is approximately equal to 0.8 m at the measurement frequency of 3.6 GHz. The results illustrated in Fig. 10-14 are all obtained based on the experimental layout shown in Fig. 9.

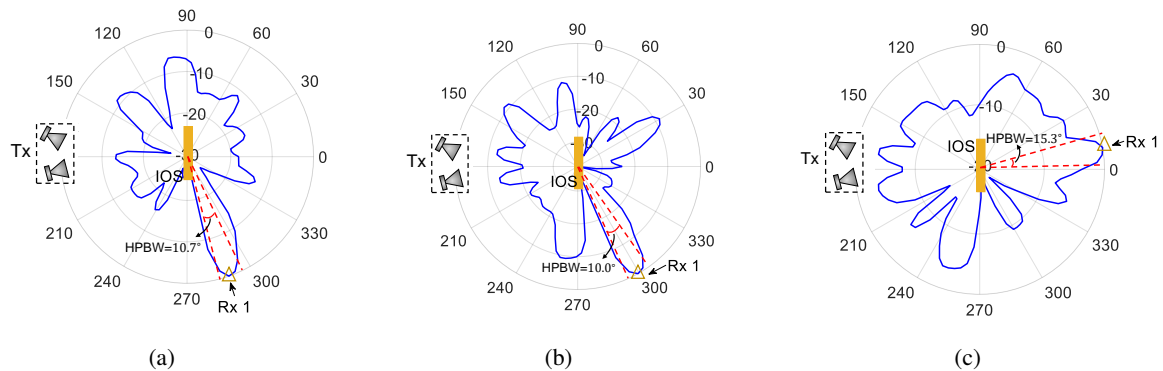


Fig. 10. Scattered beams when the IOS is configured to point towards the refraction region. In (a), (b), and (c), the beam is directed towards 289° , 299° , and 10° , respectively.

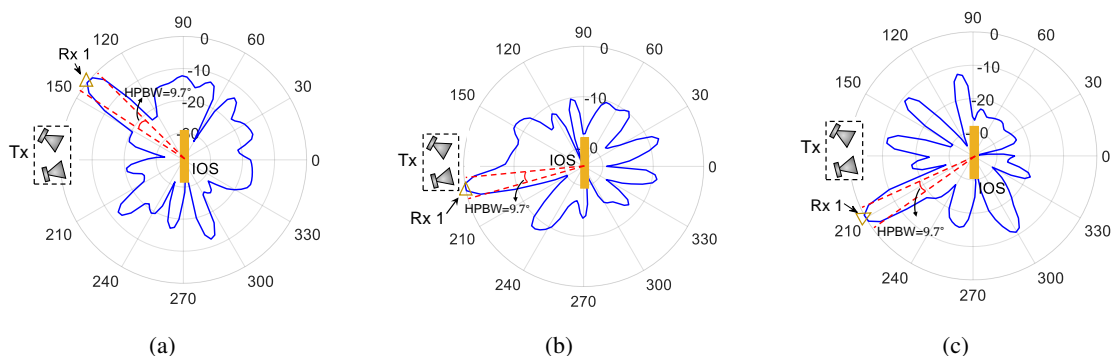


Fig. 11. Scattered beams when the IOS is configured to point towards the reflection region. In (a), (b), and (c), the beam is directed towards 141° , 188° , and 208° , respectively.

The measured radiation patterns are illustrated in Fig. 10 and Fig. 11 when the IOS is configured to steer the beam towards the refraction and reflection regions, respectively. In the figures, we see that the IOS prototype offers a narrow HPBW of about 10° and that the main lobe is directed towards the desired direction.

In Fig. 12, we evaluate the SLL of the reradiated beam when the IOS steers the signal towards the intended receiver, which can be located in the reflection and refraction sides of the surface. We see that the SLL highly depends on the desired angle of departure, i.e., reradiation. The IOS prototype offers very good SLL performance when the angle of reradiation lies in $[-60^\circ, -40^\circ]$, for both reflection and refraction. The experimental characterization in Fig. 12 provides important information on the deployment and the association between IOSs and UEs. If, for example, several IOSs are deployed in the network (see, e.g., [8]), the UEs may be associated to the IOS that offers the lowest SLL while ensuring that correct steering of the main lobe.

In Fig. 13, we illustrate the scattering efficiency of the IOS prototype as a function of the angle

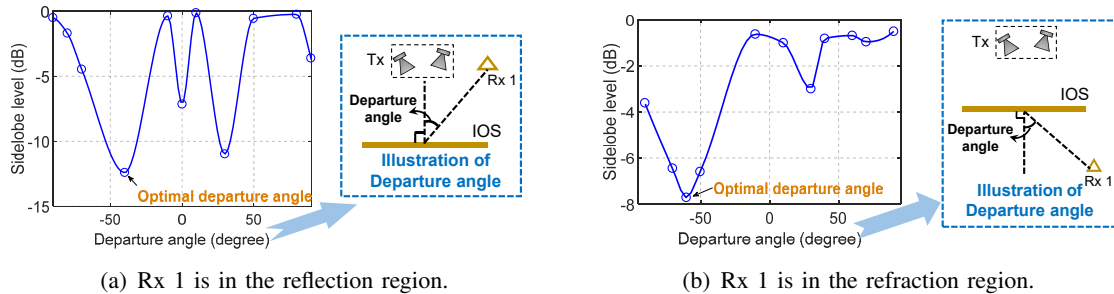


Fig. 12. Sidelobe level vs. the angle of departure from the IOS, when the scattered beam points towards the desired receiver (Rx 1). The angle of departure coincides with the angle of reflection or the angle of refraction, depending on the location of Rx 1.

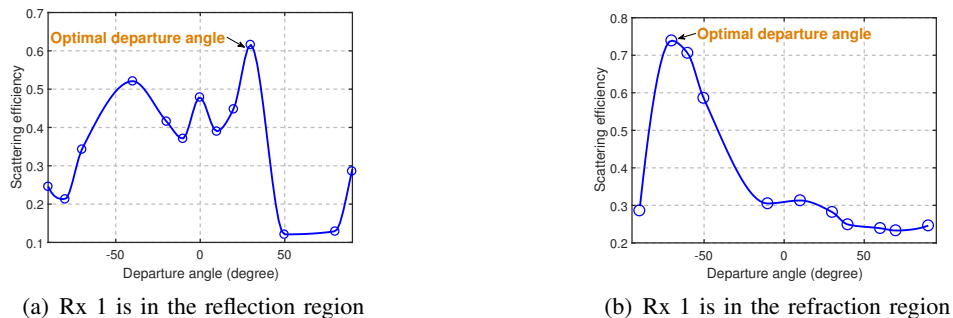


Fig. 13. Scattering efficiency vs. the angle of departure from the IOS.

TABLE II. Simulation parameters for Fig. 14

Parameters	Values
Part number of Tx antennas	LB-880
Part number of the Rx antenna	Cylindrical antenna with a gain of 3 dBi
Size of IOS	8 rows and 5 columns with 40 elements
Structure of IOS elements	As shown in Section II-C
Grouping strategy of the IOS	8 groups, each with one row of IOS elements
Deployments of Tx antennas, Rx antenna 1, and the IOS	As shown in Fig. 9

of departure (in the reflection and refraction regions). We observe a significant dependency with the target angle of departure. In the reflection region, the efficiency is maximized for angles that lie in the range $[20^\circ, 40^\circ]$. In the refraction region, the efficiency is maximized for angles that lie in the range $[-80^\circ, -60^\circ]$. This information can also be utilized to appropriately associate the UEs that are distributed throughout the network with the available IOSs.

To further demonstrate the importance of characterizing the impact of the angle of incidence on the steering capabilities of the IOS, we compare the beam patterns by taking or not taking

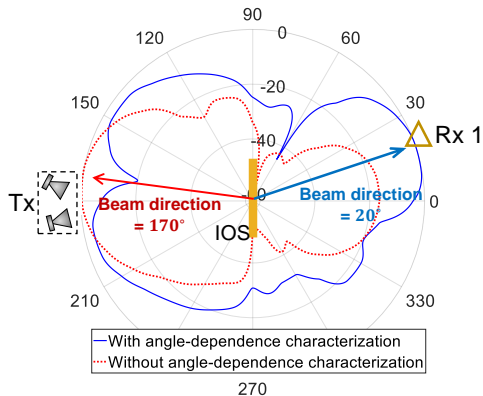


Fig. 14. Comparison of the scattered beams when the angle-dependence response of the IOS is or is not considered.

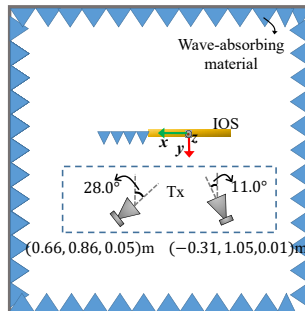


Fig. 15. Experimental layout for measuring the data rate. The figure shows the position of the two transmit antennas.

into account the angle-dependent behavior of the reflection and transmission coefficients in (7d). The simulation parameters are summarized in Table II. The results are illustrated in Fig. 14. Specifically, the curve that accounts for the impact of the angle of incidence is obtained by solving the optimization problem in (7) when imposing the angle-dependent constraint in (7d). The curve that does not account for the impact of the angle of incidence is, on the other hand, obtained by replacing the constraint in (7d) with $(\Gamma_r^{m,k}, \Gamma_t^{m,k}) \in \{(\Gamma_r(0, 0, s_m), \Gamma_t(0, 0, s_m))\}_{s_m \in \mathcal{S}}, \forall m$. In other words, as a case study, the reflection and transmission coefficients that correspond to normal incidence are utilized. Figure 14 shows that the obtained radiation patterns are different, and that the directions of the corresponding main lobes (i.e., the beam directions) are different from each other as well. This result proves the importance of utilizing appropriate EM models for optimizing IOSs.

B. Analysis of the Data Rate

In this section, we analyze the data rate of the implemented IOS-aided multi-user system. For this study, we consider the *entire* IOS prototype, which is deployed within a room whose walls are made of aluminum, in order to reduce the impact of external EM interference, and are coated with wave absorbing material, in order to avoid undesired reflections. The experimental layout,

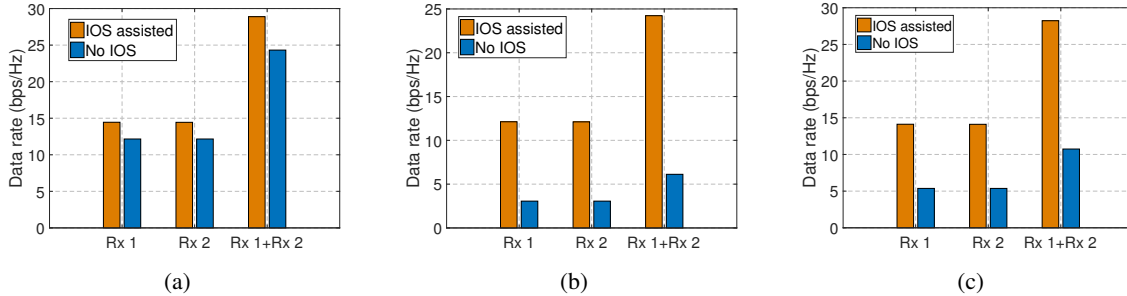


Fig. 16. Data rate of the prototype, where (a) both Rx's are in the reflection region, (b) both Rx's are in the refraction region, and (c) one Rx is located in the reflection region and one Rx is located in the refraction region.

and the positions and orientations of the transmit antennas with respect to the IOS are illustrated in Fig. 15. To simplify the control circuit, the elements of the IOS are split into 16 groups. Each group comprises 5×8 IOS elements, which are all set to the same state. The SINR threshold γ_{th} is set to 6 dB, which is in agreement with other research works [48]. To analyze the full-dimensional communication capabilities of the IOS, three different deployments for the receivers are considered: 1) Two receivers are placed in the reflection region of the IOS at the locations (0.22, 1.17, -0.24) m and (1.06, 0.49, -0.24) m, 2) two receivers are in the refraction region at the locations (0.22, -0.97, -0.24) m and (1.06, -0.49, -0.24) m, and 3) one receiver is located in the reflection region of the IOS and one receiver is located in the refraction region at the locations (0.22, 1.17, -0.24) m and (1.06, -0.49, -0.24) m, respectively. Since the Fraunhofer far-field distance of the entire IOS is approximately equal to 15.36 m at 3.6 GHz, the three considered deployments correspond to transmitters and receivers located in the radiative near-field region of the IOS. The experimental data rate obtained with the prototype is illustrated in Figs. 16 and Fig. 18, and the simulated data rate obtained with the aid of simulations is displayed in Fig. 17. In the considered scenario, specifically, the objective function in (7a) is the minimum of the data rate of the two receivers.

From Fig. 16, we evince that the data rate can be significantly increased in the presence of an IOS. We see that the two receivers, regardless of their location with respect to the IOS, can achieve a similar data rate. This is because the minimum of the data rate of the two receivers is considered as the utility function. The setup in the absence of IOS (i.e., “No IOS”) is obtained by covering the IOS with wave absorbing material. In agreement with Figs. 4 and 6, the receivers in the refraction region obtain a more pronounced improvement of the data rate with respect to the “No IOS” case, thanks to the stronger transmission coefficient.

TABLE III. Simulation parameters for Fig. 17

Parameters	Values
Part number of Tx antennas	LB-880
Part number of the Rx antenna	Cylindrical antenna with a gain of 3 dBi
Size of IOS	32 rows and 20 columns with 640 elements
Structure of IOS elements	As shown in Section II-C
Grouping strategy	16 groups of IOS elements, each with 8 rows and 5 columns
Deployments of Tx antennas and the IOS	As shown in Fig. 15
Noise power	-96 dBm
Maximum transmit power for each antenna	200 mW
Pathloss exponent	2
Carrier frequency	3.6 GHz

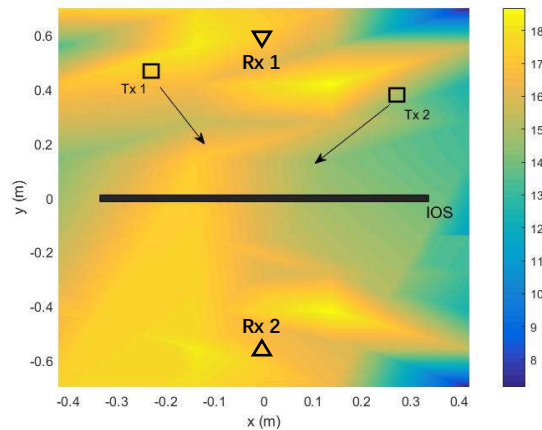


Fig. 17. Data rate distribution in the reflection and refraction sides of the IOS.

In Fig. 17, we report simulation results that illustrate the data rate distribution, in the radiative near-field region of the IOS across an area of approximate size equal to 1.2×0.8 square meters. The two receivers are located in the positions $(x, y, -0.24)$ m and $(x, -y, -0.24)$ m, where (x, y) lie in the region depicted in Fig. 17. Other simulation parameters are given in Table III. The data rate is calculated at every point (x, y) and is illustrated as a color map. We see that a good data rate is obtained around the two receivers.

In Fig. 18, we record the minimum data rate between the two Rxs as a function of the size of the IOS. The transmitters are deployed as illustrated in Fig. 15. The two receivers are located in the positions $(1.06, 0.49, -0.24)$ m and $(0.11, 0.97, -0.24)$ m, respectively. From Fig. 18, we find that the data rate is positively correlated with the size of the IOS. This is because a larger

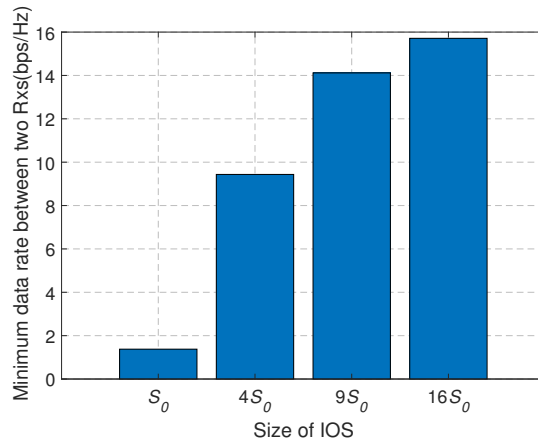


Fig. 18. Minimum data rate of two Rxs vs. the size of IOS, with $S_0 = 14.35 \times 11.36 \text{ cm}^2$.

IOS can capture more transmitted power.

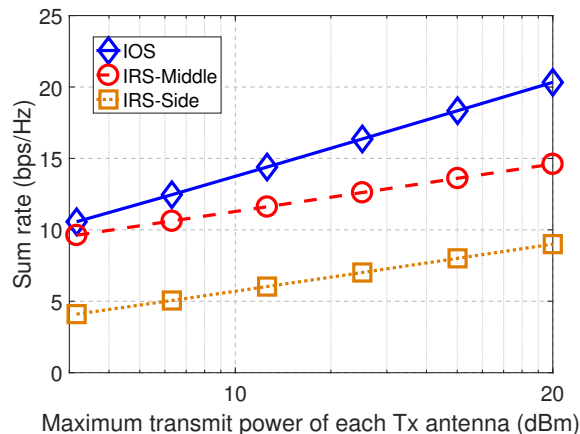


Fig. 19. Comparison of sum rate between IOS and IRS.

In Fig. 19, we compare the sum rate achieved by the IOS against the sum rate of the reflective-type RIS (IRS). To demonstrate the advantage of the IOS, two deployments for the IRS are considered: (1) *IRS-Middle*: the location of the IRS is the same as that of the IOS, and the Rxs are located on two sides of the surface (2) *IRS-Side*: the IRS is deployed such that all the Rxs and the Tx are located on the same side of the BS. For all the schemes, we assume that the direct links between the Tx and the Rxs are blocked. The other simulation parameters are listed in Table IV. As shown in Fig. 19, we see, for all the considered schemes, that the sum rate is positively correlated with the transmit power. Besides, it is observed that, compared with the *IRS-Middle* scheme, the IOS achieves a higher sum rate, since the Rxs on both sides of the

TABLE IV. Simulation Parameters

Parameters	Values
Part number of Tx antennas	LB-880
Part number of the Rx antenna	Omni-directional with a gain of 3 dBi
Size of IOS and IRS	32 rows and 20 columns with 640 elements
Structure of IOS elements	As shown in Section II-C
Size and radiation efficiency of IRS elements	The same as the IOS elements
Grouping strategy	16 groups of metasurface elements, each with 8 rows and 5 columns
Deployments of Tx antennas	Tx antenna 1: (0.66, 0.86, 2) m, Tx antenna 2: (-0.31, 1.05, 2) m
Deployments of Rxs	Rx 1: (0.4, 1.2, -0.24) m, Rx 2: (-0.6, -1, -0.24) m
Deployment of IOS	On the xoz plane with its center coincides with the origin
Deployment of IRS in IRS-Middle scheme	On the xoz plane with its center coincides with the origin
Deployment of IRS in IRS-Side scheme	Parallel to the $yo z$ plane, and the coordinate of its center is (-1, 0, 0) m
Noise power	-90 dBm
Carrier frequency	3.6 GHz

surface can be served. In addition, the IOS also outperforms the IRS-Side scheme, indicating that the IOS can be appropriately optimized to outperform the IRS.

VII. CONCLUSION

In this paper, we have proposed a new reflection-refraction model for the reconfigurable elements of IOSs. The circuit-based model has been verified through full-wave EM simulations. Based on the obtained equivalent circuit model, we have demonstrated the influence of the angle of incidence and the IOS structure on the reflection and transmission coefficients. Also, we have studied the asymmetry between the reflection and transmission coefficients. Moreover, the proposed circuit-based model has been integrated into a mathematical framework for jointly optimizing the digital beamformer at the transmitter and the analog beamformer at the IOS. To verify the theoretical findings and evaluate the performance of the full-dimensional beamforming, we have implemented an IOS hardware prototype and have deployed an IOS-assisted wireless

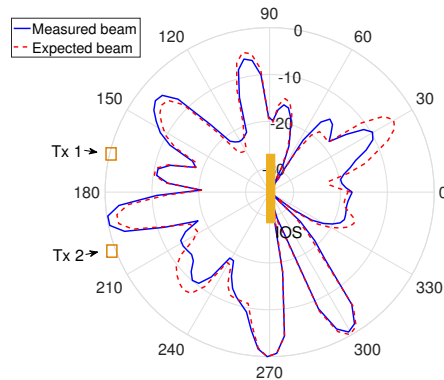


Fig. 20. Comparison between measured and expected scattered beams.

communication testbed, and have experimentally characterized the beam pattern of the IOS and the achievable rate. Based on the proposed equivalent circuit model and the experiments conducted, the following main conclusions are obtained:

- The angle of incidence has a non-negligible impact on the reflection and transmission coefficients, which should be taken into account in the hybrid beamforming design for improving the system performance.
- In network deployments in which multiple IOSs and receivers are available, the receivers should communicate with the aid of the IOS that corresponds to a moderate angle of reradiation. This configuration helps reduce the SLL and helps improve the scattering efficiency, which in turn is beneficial for full-dimensional communications.
- The experimental results show that the IOS can steer the reflected and refracted far-field beams over 360° . Also, ubiquitous coverage can be obtained in the radiative near-field region as well.

APPENDIX A

VERIFICATION OF THE MODEL FOR THE SCATTERED BEAM IN (8)

To demonstrate the validity of the model for the scattered beam in (8), we select a specific IOS configuration and a given digital beamformer, and measure the corresponding scattered beam. In Fig. 20, we compare the measured scattered beam and the expected scattered beam based on (8). We see that the measured beam matches well with the expected beam, which indicates that the scattered beam can be predicted with the proposed model in (8).

REFERENCES

- [1] Ericsson White Paper, “More than 50 billion connected devices,” Utah Education Network, Salt Lake City, UT, Tech. Rep. 284 23-3149, Feb. 2011.

- [2] M. Di Renzo, H. Haas, A. Ghayeb, S. Sugiura, and L. Hanzo, "Spatial modulation for generalized MIMO: Challenges, opportunities, and implementation," *Proc. IEEE*, vol. 102, no. 1, pp. 56-103, Jan. 2014.
- [3] E. G. Larsson, O. Edfors, F. Tufvesson, and T. L. Marzetta, "Massive MIMO for next generation wireless systems," *IEEE Commun. Mag.*, vol. 52, no. 2, pp. 186-195, Feb. 2014.
- [4] M. Di Renzo, et. al., "Smart radio environments empowered by reconfigurable intelligent surfaces: How it works, state of research, and the road ahead," *IEEE J. Sel. Areas Commun.*, vol. 38, no. 11, pp. 2450-2525, Nov. 2020.
- [5] Y. Liang, et. al., "Reconfigurable intelligent surfaces for smart wireless environments: Channel estimation, system design and applications in 6G networks," *Sci. China Inf. Sci.*, vol. 1, no. 1, pp. 1-21, Jul 2021.
- [6] Q. Li, M. Wen, and M. Di Renzo, "Single-RF MIMO: From spatial modulation to metasurface-based modulation," *IEEE Wireless Commun.*, vol. 28, no. 4, pp. 88-95, Aug. 2021.
- [7] Gabriele Gradoni, et. al., "Smart radio environments," [online]. Available: <https://arxiv.org/abs/2111.08676>.
- [8] B. Sihlbom, M. I. Poulakis, and M. Di Renzo, "Reconfigurable intelligent surfaces: Performance assessment through a system-level simulator," [online]. Available: <https://arxiv.org/abs/2111.10791>
- [9] H. Zhang, B. Di, L. Song, and Z. Han, *Reconfigurable Intelligent Surface-Empowered 6G*, Switzerland, Springer Nature Switzerland AG, 2021.
- [10] T. V. Chien, H. Q. Ngo, S. Chatzinotas, M. Di Renzo, and B. Ottersten, "Reconfigurable intelligent surface-assisted cell-free massive MIMO systems over spatially-correlated channels," *IEEE Trans. Wireless Commun.*, to be published.
- [11] M. Di Renzo, M. Debbah, D. Phan-Huy, A. Zappone, M. Alouini, C. Yuen, V. Sciancalepore, G. C. Alexandropoulos, J. Hoydis, H. Gacanin, J. Rosny, A. Bounceur, G. Lerosey, and M. Fink, "Smart radio environments empowered by reconfigurable AI meta-surfaces: An idea whose time has come," *EURASIP J. Wireless Commun. Netw.*, vol. 2019, no. 129, pp. 1-20, May 2019.
- [12] B. Di, H. Zhang, L. Song, Y. Li, Z. Han, and H. V. Poor, "Hybrid beamforming for reconfigurable intelligent surface based multi-user communications: Achievable rates with limited discrete phase shifts," *IEEE J. Sel. Areas Commun.*, vol. 38, no. 8, pp. 1809-1822, Aug. 2020.
- [13] M. Di Renzo, F. H. Danufane, and S. Tretyakov, "Communication models for reconfigurable intelligent surfaces: From surface electromagnetics to wireless networks optimization," [online]. Available: <https://arxiv.org/abs/2110.00833>.
- [14] L. Dai, et. al., "Reconfigurable intelligent surface-based wireless communications: Antenna design, prototyping, and experimental results," *IEEE Access*, vol. 8, no. 1, pp. 45913-45923, Mar. 2020.
- [15] R. Fara, P. Ratajczak, D.-T. P. Huy, A. Ourir, M. Di Renzo, and J. de Rosny, "A prototype of reconfigurable intelligent surface with continuous control of the reflection phase," *IEEE Wireless Commun. Mag.*, (to be published).
- [16] S. Zeng, H. Zhang, B. Di, Z. Han, and L. Song, "Reconfigurable intelligent surface (RIS) assisted wireless coverage extension: RIS orientation and location optimization," *IEEE Commun. Lett.*, vol. 25, no. 1, pp. 269-273, Jan. 2021.
- [17] M. A. Elmoallamy, H. Zhang, L. Song, K. Seddik, Z. Han, and G. Y. Li, "Reconfigurable intelligent surfaces for wireless communications: Principles, challenges, and opportunities," *IEEE Trans. Cognitive Commun. Netw.*, vol. 6, no. 3, pp. 990-1002, Sep. 2020.
- [18] W. Tang, M. Chen, X. Chen, J. Dai, Y. Han, M. Di Renzo, Y. Zeng, S. Jin, Q. Cheng, and T. Cui, "Wireless communications with reconfigurable intelligent surface: Path loss modeling and experimental measurement," *IEEE Trans. Wireless Commun.*, vol. 20, no. 1, pp. 421-439, Jan. 2021.
- [19] M. Dunna, C. Zhang, D. Sievenpiper, and D. Bharadia, "ScatterMIMO: Enabling virtual MIMO with smart surfaces," in *Proc. MobiCom '20*, London, U.K., Sept. 2020, pp. 1-14.
- [20] K. Cho, M. Mazaheri, J. Gummesson, O. Abari, and K. Jamieson, "mmWall: A reconfigurable metamaterial surface for mmWave networks," in *Proc. HotMobile '21*, U.K., Feb. 2021, pp. 1-7.

- [21] H. Zhang, B. Di, K. Bian, Z. Han, H. V. Poor, and L. Song, "Toward ubiquitous sensing and localization with reconfigurable intelligent surfaces," *Proc. IEEE*, to be published.
- [22] S. Zhang, H. Zhang, B. Di, Y. Tan, M. Di Renzo, Z. Han, H. V. Poor, and L. Song, "Intelligent Omni-Surface: Ubiquitous wireless transmission by reflective-refractive metasurfaces," *IEEE Trans. Wireless Commun.*, vol. 21, no. 1, pp. 219-233, Jan. 2022.
- [23] J. Xu, Y. Liu, X. Mu, J. T. Zhou, L. Song, H. V. Poor, and L. Hanzo, "Simultaneously transmitting and reflecting (STAR) intelligent omni-surfaces, their modeling and implementation," [online]. Available: <https://arxiv.org/abs/2108.06233>.
- [24] Y. Liu et al., "STAR: Simultaneous transmission and reflection for 360° coverage by intelligent surfaces," *IEEE Wireless Commun.*, vol. 28, no. 6, pp. 102-109, Dec. 2021.
- [25] H. Zhang, S. Zeng, B. Di, Y. Tan, M. Di Renzo, M. Debbah, L. Song, Z. Han, and H. V. Poor, "Intelligent omni-surfaces for full-dimensional wireless communications principle, technology, and implementation," *IEEE Commun. Mag.*, vol. 60, no. 2, pp. 39-45, Feb. 2022.
- [26] Y. Zhang, B. Di, H. Zhang, Z. Han, H. V. Poor, and L. Song, "Meta-Wall: Intelligent omni-surfaces aided multi-cell MIMO communications," *IEEE Trans. Wireless Commun.*, to be published.
- [27] C. Wu, Y. Liu, X. Mu, X. Gu, and O. A. Dobre, "Coverage characterization of STAR-RIS networks: NOMA and OMA," *IEEE Comm. Lett.*, vol. 25, no. 9, pp. 3134-3138, Sep. 2021.
- [28] S. Zeng, H. Zhang, B. Di, Y. Tan, Z. Han, H. V. Poor, and L. Song, "Reconfigurable intelligent surfaces in 6G: Reflective, transmissive, or both," *IEEE Commun. Lett.*, vol. 25, no. 6, pp. 2063-2067, Feb. 2021.
- [29] C. Zhang, W. Yi, Y. Liu, Z. Ding, and L. Song, "STAR-IOS aided NOMA networks: Channel model approximation and performance analysis," [online]: <https://arxiv.org/pdf/2107.01543.pdf>
- [30] J. Xu, Y. Liu, X. Mu, and O. A. Dobre, "STAR-RISs: Simultaneous transmitting and reflecting reconfigurable intelligent surfaces," *IEEE Comm. Lett.*, vol. 25, no. 9, pp. 3134-3138, Sept. 2021.
- [31] V. Torres, F. Mesa, M. Navarro-Cía, R. Rodríguez-Berral, M. Beruete, and F. Medina, "Accurate circuit modeling of fishnet structures for negative-index-medium applications," *IEEE Trans. Microw. Theory Tech.*, vol. 64, no. 1, pp. 15-26, Jan. 2016.
- [32] M. Kafesaki, I. Tsiapa, N. Katsarakis, Th. Koschny, C. Soukoulis, and E. Economou, "Left-handed metamaterials: The fishnet structure and its variations," *Phys. Rev. B*, vol. 1, no. 1, pp. 1-9, Jun. 2007.
- [33] F. Costa, A. Monorchio, and G. Manara, "An overview of equivalent circuit modeling techniques of frequency selective surfaces and metasurfaces," *Appl. Comput. Electromagn. Soc. J.*, vol. 29, no. 12, pp. 1-15, Dec. 2014.
- [34] L. Li, H. Ruan, C. Liu, Y. Li, Y. Shuang, A. Alu, C. Qiu, and T. Cui, "Machine-learning reprogrammable metasurface imager," *Nat. Comm.*, vol. 10, no. 1, pp. 1-9, Mar. 2019.
- [35] D. M. Pozar, *Microwave Engineering (3th Edition)*, New York, John Wiley & Sons, 2005.
- [36] M. Di Renzo, A. Ahmed, A. Zappone, V. Galdi, G. Gradoni, M. Moccia, and G. Castaldi, "Digital reconfigurable intelligent surfaces: On the impact of realistic reradiation models", [online]. Available: <https://arxiv.org/abs/2205.09799>.
- [37] T. Cui, M. Qi, X. Wan, J. Zhao, and Q. Cheng, "Coding metamaterials, digital metamaterials and programmable metamaterials," *Light Sci. Appl.*, vol. 3, no. 10, pp. 1-9, Sep. 2014.
- [38] A. Albanese, F. Devoti, V. Sciancalepore, M. Di Renzo, X. Costa-Perez, "MARISA: A self-configuring metasurfaces absorption and reflection solution towards 6G," in *Proc. IEEE INFOCOM*, to be published.
- [39] S. Zhang, H. Zhang, B. Di, Y. Tan, M. Di Renzo, Z. Han, and L. Song, "Beyond intelligent reflecting surfaces: Reflective-transmissive metasurface aided communications for full-dimensional coverage extension," *IEEE Trans. Veh. Tech.*, vol. 69, no. 11, pp. 13905-13909, Nov. 2020.
- [40] F. Rusek, D. Persson, B. K. Lau, E. G. Larsson, T. L. Marzetta, and F. Tufvesson, "Scaling up MIMO: Opportunities and challenges with very large arrays," *IEEE Signal Process. Mag.*, vol. 30, no. 1, pp. 40-60, Jan. 2013.

- [41] W. Yang, Q. Meng, W. Che, L. Gu, and Q. Xue, "Low-profile wideband dual-circularly polarized metasurface antenna array with large beamwidth," *IEEE Antennas Wirel. Propag. Lett.*, vol. 17, no. 9, pp. 1613-1616, Sep. 2018.
- [42] Q. Zheng, Y. Li, Y. Han, Y. Jing, M. Feng, Y. Pang, J. Wang, H. Ma, S. Qu, and J. Zhang, "Ultra-wideband side-lobe level suppression using amplitude-adjustable metasurfaces," *J. Phys. D: Appl. Phys.*, vol. 1, no. 1, pp. 1-7, Dec. 2018.
- [43] V. Popov, B. Ratni, S. N. Burokur, and F. Boust, "Non-local reconfigurable sparse metasurface: Efficient near-field and far-field wavefront manipulations," *Adv. Opt. Mater.*, vol. 9, no. 4, pp. 1-11, Jan. 2021.
- [44] J. Hu, H. Zhang, B. Di, L. Li, K. Bian, L. Song, Y. Li, Z. Han, and H. V. Poor, "Reconfigurable intelligent surface based RF sensing: Design, optimization, and implementation," *IEEE J. Sel. Areas Commun.*, vol. 38, no. 11, pp. 2700-2716, Nov. 2020.
- [45] M. Ettus, and M. Braun, "The Universal software radio peripheral (USRP) family of low-cost SDRs," *Opportunistic Spectr. Sharing White Space Access: The Practical Reality*, pp. 3-23, Jul. 2015.
- [46] Y. Zhang, B. Di, H. Zhang, M. Dong, L. Yang, and L. Song, "Dual codebook design for intelligent omni-surface aided communications," *IEEE Trans. Wireless Commun.*, to be published.
- [47] R. J. Larsen, and M. L. Marx, *An Introduction to Mathematical Statistics and Its Applications*. Boston, the U.S.: Pearson Education, 2012.
- [48] M. Elhattab, M. A. Arfaoui, C. Assi, and A. Ghayeb, "RIS-assisted joint transmission in a two-cell downlink NOMA cellular system," *IEEE J. Sel. Areas Commun.*, vol. 40, no. 4, pp. 1270-1286, April 2022.